OPEN ACCESS



Comprehensive Radio Monitoring of the Black Hole X-Ray Binary Swift J1727.8—1613 during Its 2023–2024 Outburst

```
Andrew K. Hughes <sup>1</sup>, Francesco Carotenuto <sup>2</sup>, Thomas D. Russell <sup>3</sup>, Alexandra J. Tetarenko <sup>4</sup>, James C. A. Miller-Jones <sup>5</sup>,
  Arash Bahramian<sup>5</sup>, Joe S. Bright<sup>1,6</sup>, Fraser J. Cowie<sup>1</sup>, Rob Fender<sup>1,7</sup>, Mark A. Gurwell<sup>8</sup>, Jasvinderjit K. Khaulsay<sup>9</sup>, Anastasia Kirby<sup>5</sup>, Serena Jones<sup>5</sup>, Elodie Lescure<sup>4</sup>, Michael McCollough<sup>8</sup>, Richard M. Plotkin<sup>10,11</sup>, Ramprasad Rao<sup>8</sup>,
Saeqa D. Vrtilek<sup>8</sup>, David R. A. Williams-Baldwin<sup>12</sup>, Callan M. Wood<sup>5</sup>, Gregory R. Sivakoff<sup>13</sup>, Diego Altamirano<sup>14</sup>,
 Piergiorgio Casella<sup>2</sup>, Stéphane Corbel<sup>15</sup>, David R. DeBoer<sup>16</sup>, Melania Del Santo<sup>3</sup>, Constanza Echiburú-Trujillo<sup>17</sup>, Wael Farah<sup>18</sup>, Poshak Gandhi<sup>14</sup>, Karri I. I. Koljonen<sup>19</sup>, Thomas Maccarone<sup>20</sup>, James H. Matthews<sup>1</sup>, Sera B. Markoff<sup>21,22</sup>, Alexander W. Pollak<sup>18</sup>, David M. Russell<sup>23</sup>, Payaswini Saikia<sup>23</sup>, Noel Castro Segura<sup>24</sup>, Aarran W. Shaw<sup>25</sup>, Andrew Siemion<sup>1,6,26,27,28,29</sup>, Roberto Soria<sup>30,31</sup>, John A. Tomsick<sup>32</sup>, and
                                                                           Jakob van den Eijnden<sup>21,33</sup> ©
                             <sup>1</sup> Department of Physics, University of Oxford, Denys Wilkinson Building, Keble Road, Oxford, OX1 3RH, UK
                                    INAF—Osservatorio Astronomico di Roma, Via Frascati 33, I-00076, Monte Porzio Catone (RM), Italy
                                     INAF, Istituto di Astrofisica Spaziale e Fisica Cosmica, Via U. La Malfa 153, I-90146 Palermo, Italy
                                   <sup>4</sup> Department of Physics and Astronomy, University of Lethbridge, Lethbridge, AB T1K 3M4, Canada
                         <sup>5</sup> International Centre for Radio Astronomy Research, Curtin University, GPO Box U1987, Perth, WA 6845, Australia
                     <sup>6</sup> Breakthrough Listen, Astrophysics, Department of Physics, The University of Oxford, Keble Road, Oxford, OX1 3RH, UK
                                    Department of Astronomy, University of Cape Town, Private Bag X3, Rondebosch 7701, South Africa
                                      Center for Astrophysics | Harvard & Smithsonian, 60 Garden Street, Cambridge, MA 02138, USA
                   <sup>9</sup> Department of Physics and Astronomy, The University of Sheffield, Hicks Building, Hounsfield Road, Sheffield, S3 7RH, UK
                                                         Department of Physics, University of Nevada, Reno, NV 89557, USA
                                             Nevada Center for Astrophysics, University of Nevada, Las Vegas, NV 89154, USA
                <sup>12</sup> Jodrell Bank Centre for Astrophysics, School of Physics and Astronomy, The University of Manchester, Manchester, M13 9PL, UK
                                         Department of Physics, University of Alberta, CCIS 4-181, Edmonton, AB T6G 2E1, Canada <sup>14</sup> School of Physics & Astronomy, University of Southampton, SO17 1BJ, UK
                                  <sup>15</sup> Université Paris Cité and Université Paris Saclay, CEA, CNRS, AIM, F-91190 Gif-sur-Yvette, France
                                                 Radio Astronomy Lab, University of California, Berkeley, CA 94720-3411, USA
  <sup>17</sup> Department of Astrophysical and Planetary Sciences, JILA, Duane Physics Bldg., 2000 Colorado Ave., University of Colorado, Boulder, CO 80309, USA
                                                   SETI Institute, 339 Bernardo Ave, Suite 200 Mountain View, CA 94043, USA
                                Department of Physics, Norwegian University of Science and Technology, NO-7491 Trondheim, Norway
                                         Department of Physics and Astronomy, Texas Tech University, Lubbock, TX 79409-1051, USA
                  <sup>21</sup> Anton Pannekoek Institute for Astronomy, University of Amsterdam, Science Park 904, 1098 XH Amsterdam, The Netherlands
   <sup>22</sup> Gravitation and Astroparticle Physics Amsterdam Institute, University of Amsterdam, Science Park 904, 1098 XH 195 196 Amsterdam, The Netherlands
                        Center for Astrophysics and Space Science (CASS), New York University Abu Dhabi, PO Box 129188, Abu Dhabi, UAE

Department of Physics, University of Warwick, Gibbet Hill Road, Coventry, CV 4 7AL, UK
                             Department of Physics and Astronomy, Butler University, 4600 Sunset Avenue, Indianapolis, IN 46208, USA
                                                   SETI Institute, 339 Bernardo Ave, Suite 200, Mountain View, CA 94043, USA
                                            <sup>27</sup> Berkeley SETI Research Centre, University of California, Berkeley, CA 94720, USA
                                       <sup>28</sup> Department of Physics and Astronomy, University of Manchester, Manchester, M13 9PL, UK
<sup>29</sup> University of Malta, Institute of Space Sciences and Astronomy, Msida, MSD2080, Malta
                                      30 INAF—Osservatorio Astrofisico di Torino, Strada Osservatorio 20, I-10025 Pino Torinese, Italy
                          <sup>31</sup> Sydney Institute for Astronomy, School of Physics A28, The University of Sydney, Sydney, NSW 2006, Australia
                                       Space Sciences Lab, University of California, Berkeley, 7 Gauss Way, Berkeley, CA 94720, USA
                                                      Department of Physics, University of Warwick, Coventry, CV4 7AL, UK
                                       Received 2025 March 13; revised 2025 May 23; accepted 2025 June 4; published 2025 July 17
```

Abstract

This work presents comprehensive multifrequency radio monitoring of the black hole low-mass X-ray binary (LMXB) Swift J1727.8–1613, which underwent its first recorded outburst after its discovery in 2023 August. Through a considerable community effort, we have coalesced the data from multiple, distinct observing programs; the light curves include $\sim \! 10 \!$ months and 197 epochs of monitoring from seven radio facilities with observing frequencies ranging from (approximately) 0.3–230 GHz. The primary purpose of this work is to provide the broader astronomical community with these light curves to assist with the interpretation of other observing campaigns, particularly nonradio observing frequencies. We discuss the phenomenological evolution of the source, which included (i) multiple radio flares consistent with the launching of discrete jet ejections, the brightest of which reached $\sim \! 1 \!$ Jy; (ii) temporally evolving radio spectral indices (α), reaching values steeper than expected for optically thin synchrotron emission ($\alpha < -1$) and emission with significant radiative cooling ($\alpha < -1.5$). We have published a digital copy of the data and intend for this work to set a precedent for the community to continue releasing comprehensive radio light curves of future LMXB outbursts.

Unified Astronomy Thesaurus concepts: Accretion (14); Radio continuum emission (1340); Black holes (162); Relativistic jets (1390); X-ray binary stars (1811)

Materials only available in the online version of record: machine-readable table

1. Introduction

Astrophysical jets are highly collimated outflows that are produced by nearly all accreting compact objects (black holes, neutron stars, and white dwarfs; M. Livio 2002; P. Kumar & B. Zhang 2015; R. Fender et al. 2019; F. De Colle & W. Lu 2020; M. Ruiz et al. 2021; O. Gottlieb et al. 2023). Given their ubiquity, interactions between the matter accelerated by jets and the ambient environment (i.e., "feedback") have played and continue to play a critical role in driving local evolution on even the largest of scales (e.g., M. J. Hardcastle & J. H. Croston 2020). Therefore, understanding jets is crucial for understanding the Universe as a whole. For time-domain studies, an archetypal jet "laboratory" is the black hole low-mass X-ray binary (BH LMXB).

Black hole low-mass X-ray binaries are interacting binaries composed of a stellar-mass BH ($\sim 10M_{\odot}$) accreting material from a low-mass ($\lesssim 1M_{\odot}$) companion star. Many BH LMXBs are transient in nature, spending the majority of their lifetimes accreting small amounts of matter in a quiescent low-luminosity state $(L_{\rm X} < 10^{34}\,{\rm erg\,s^{-1}})$, where $L_{\rm X}$ is the X-ray luminosity of the accretion flow; R. M. Plotkin et al. 2013). These objects may also sporadically enter into bright outbursts where their broadband emission brightens considerably. During the week-to-years-long outbursts (J. M. Corral-Santana et al. 2016; B. E. Tetarenko et al. 2016), the accretion flow (best observed at X-ray frequencies; e.g., H. Tananbaum et al. 1972; T. Belloni et al. 1999) and jets (best observed at radio-to-IR frequencies; e.g., H. Tananbaum et al. 1972; S. Corbel & R. P. Fender 2002; D. M. Russell et al. 2013; A. J. Tetarenko et al. 2017) evolve significantly as the system transitions through different empirically defined "accretion states" (see, e.g., R. P. Fender et al. 2004; J. E. McClintock & R. A. Remillard 2006; T. M. Belloni 2010).

A typical outburst begins with a rapid increase in the X-ray luminosity and a transition (from quiescence) into the hard state ($10^{35} \lesssim L_{\rm X} \lesssim 10^{39}\,{\rm erg\,s^{-1}}$). In the hard state, the X-ray spectrum is nonthermal, with the X-rays being dominated by high-energy emission (i.e., "hard" X-rays) due to Compton upscattering of seed photons by an optically thin coronal flow (K. S. Thorne & R. H. Price 1975; S. L. Shapiro et al. 1976). As the accretion rate increases, the source transitions through intermediate states: First, the hard intermediate state, followed by the soft-intermediate state, during which the X-ray emission becomes progressively softer (i.e., more dominated by lowerenergy "soft" disk photons). Eventually, the system enters the soft state, with a spectrum dominated by thermal emission from an optically thick, geometrically thin accretion disk. A BH LMXB typically remains in the soft state for weeks to months, decreasing in X-ray luminosity before transitioning back to the hard state through lower-luminosity intermediate states and finally returning to quiescence (see, e.g., J. Homan & T. Belloni 2005; J. E. McClintock & R. A. Remillard 2006; T. M. Belloni 2010; A. R. Ingram & S. E. Motta 2019; E. Kalemci et al. 2022, for a comprehensive description of the accretion states).

.The properties of relativistic jets evolve with the accretion states (see, e.g., R. P. Fender et al. 2004, 2009; R. Fender 2010, for detailed reviews). In the hard state, a continuously accelerated

jet is launched (henceforth the "compact jet"), typically described with the stratified, conical outflow model of R. D. Blandford & A. Königl (1979). Compact jets exhibit an optically thick, partially self-absorbed synchrotron spectrum with a (typically) flat or mildly inverted spectral index ($\alpha \gtrsim 0$; the flux density, $F_{R,\nu}$, is proportional to the observing frequency, ν , such that $F_{R,\nu} \propto \nu^{\alpha}$) up to a break frequency where the spectrum becomes optically thin ($\alpha \sim -0.6$, typically in the submillimeter or near-IR regimes; S. Migliari et al. 2010; D. M. Russell et al. 2013; T. D. Russell et al. 2014). The radio luminosity from the compact jet shows a strong, positive correlation with X-ray luminosity from the accretion flow (e.g., E. Gallo et al. 2003; S. Corbel et al. 2013; E. Gallo et al. 2018), consistent with continuous accretion-jet coupling in the hard state.

Monitoring campaigns following state transitions have captured ≥3 orders of magnitude decreases in radio luminosity, showing that compact jets are strongly quenched in the soft state (e.g., R. Fender et al. 1999; M. Coriat et al. 2011; T. D. Russell et al. 2019, 2020; J. S. Bright et al. 2020; T. J. Maccarone et al. 2020; F. Carotenuto et al. 2021). Around this time, bright radio flares can be observed around the hard-to-soft state transition (e.g., A. J. Tetarenko et al. 2017). These flares are associated with the launching of mildly to extremely relativistically bipolar ejecta, decoupling the jets from the accretion flow (e.g., I. F. Mirabel & L. F. Rodríguez 1994; R. M. Hjellming & M. P. Rupen 1995; R. P. Fender et al. 1999; C. Brocksopp et al. 2002; S. Corbel et al. 2002; A. P. Rushton et al. 2017; J. C. A. Miller-Jones et al. 2019; T. D. Russell et al. 2019; J. S. Bright et al. 2020; F. Carotenuto et al. 2021; C. M. Wood et al. 2021). The radio spectra of the flares evolve rapidly in time, transitioning from optically thick to optically thin synchrotron emission as the emitting plasma expands, causing a decrease in the self-absorption frequency (e.g., H. van der Laan 1966; R. M. Hjellming & K. J. Johnston 1988; R. Fender & J. Bright 2019). As a result, for the majority of their lifetimes (including when they are spatially resolvable), ejecta are optically thin radio sources.

Jet ejecta can be detected from minutes to even years after launch (e.g., S. Corbel et al. 2002; J. C. A. Miller-Jones et al. 2019; C. M. Wood et al. 2021; A. Bahramian et al. 2023). An observational consequence is that radio emission can be detected in the soft state despite the compact jet being quenched. The longest-lasting ejecta are believed to remain bright because of the continual acceleration of particles driven by interactions with the ambient interstellar medium (ISM; S. Corbel et al. 2002; T. D. Russell et al. 2019; J. S. Bright et al. 2020; M. Espinasse et al. 2020; F. Carotenuto et al. 2021), where some BH LMXB jets produce interaction regions tens of parsecs away from the BH (e.g., A. J. Tetarenko et al. 2018). In extreme cases, ejecta that have faded below the detection threshold can remain undetected for months or years before rebrightening during jet-ISM interactions (e.g., S. Corbel et al. 2002; F. Carotenuto et al. 2021).

While there is some phenomenological understanding of the evolution of the jets through the BH LMXB accretion states, knowledge of the precise timings and causal sequence of events leading to jet quenching and transient jet launching, or

the intrinsic properties such as total energy content (and thus total energy available for feedback) is far from complete. Each subsequent BH LMXB outburst provides (often multiple) new opportunities for real-time monitoring of jet launching, disruption, and interaction events, and thus a chance to test and refine our current understanding. Moreover, multiwavelength observations allow us to probe the connection between jets and the accretion flow, jets and other outflows (e.g., winds; J. Sánchez-Sierras & T. Muñoz-Darias 2020), or investigate how jet properties change with the observing frequency (D. M. Russell et al. 2006). Naturally, bright outbursts provide the highest-quality monitoring, but only if the observing campaigns are sufficient to build a coherent picture. One such opportunity arose in 2023 when the BH LMXB Swift J1727.8 –1613 began a bright outburst.

1.1. The 2023-2024 Outburst of Swift J1727.8-1613

Swift J1727.8–1613 (hereafter Swift J1727) was discovered on 2023 August 24 (MJD 60180) by the Burst Alert Telescope (S. D. Barthelmy et al. 2005; H. A. Krimm et al. 2013) on board the Neil Gehrels Swift Observatory (N. Gehrels et al. 2004). Within days, the source's X-ray flux reached ~7 Crab (at 2–20 keV), resulting in its initial classification as a gammaray burst (GRB 230824A; K. L. Page et al. 2023). Follow-up X-ray observations refuted a GRB origin, reclassifying (and renaming) the source as the Galactic transient Swift J1727 (J. A. Kennea & Swift Team 2023). The rapid rise in X-ray luminosity motivated extensive multiwavelength monitoring and identified Swift J1727 as a BH LMXB (D. Mata Sánchez et al. 2025).

Rapid radio follow-up localized the source with subarcsecond precision (J2000), $17^{\text{h}}27^{\text{m}}43.31 \ (\pm 0^{\text{s}}.04), -16^{\circ}12^{'}19.23 \ (\pm 0^{''}.02)$ (J. C. A. Miller-Jones et al. 2023b). Multi-epoch optical spectroscopy by D. Mata Sánchez et al. (2024) estimated the properties of the companion star, favoring an early K-type companion star with an \sim 8 hr orbital period. D. Mata Sánchez et al. (2024) used the orbital period and observed optical extinction to estimate an initial distance of $2.7 \pm 0.3 \,\mathrm{kpc}$; D. Mata Sánchez et al. (2025) refined the orbital period, calculated a new distance of 3.7 \pm 0.3 kpc, and dynamically confirmed that Swift J1727 contained a stellar-mass BH. The most recent analysis of optical (and near-UV) extinction by B. J. Burridge et al. (2025) reviewed the systematics in D. Mata Sánchez et al. (2025) and favored a larger distance of $5.5^{+1.4}_{-1.1}$ kpc. X-ray spectral modeling revealed relativistically broadened iron lines, suggestive of a highspin ($a \sim 0.98$), medium-inclination system ($\sim 40^{\circ}$ –50° inclination angle; P. A. Draghis et al. 2023; J.-Q. Peng et al. 2024). Subsequent modeling, which also considered the X-ray polarization properties, found a similar inclination angle ($\sim 30^{\circ}-50^{\circ}$) but favored a lower spin ($a \sim 0.87$; J. Svoboda et al. 2024).

The initial rise in X-ray luminosity occurred as Swift J1727 exhibited X-ray and radio properties characteristic of the hard accretion state (e.g., N. Bollemeijer et al. 2023a; J. C. A. Miller-Jones et al. 2023b; H.-X. Liu et al. 2024; I. Mereminskiy et al. 2024; J.-Q. Peng et al. 2024); direct imaging of the compact jet revealed Swift J1727 to have the largest resolved compact jet seen from a BH LMXB (C. M. Wood et al. 2024). As Swift J1727 evolved (through the hard intermediate state), X-ray monitoring suggested the source transitioned to a soft-intermediate or soft state on 2024 October 5 (MJD 60222, although X-ray observations were unable to discriminate between the states; N. Bollemeijer et al. 2023a, 2023b). Radio quenching

accompanied the X-ray transition, followed by bright (radio) flaring, consistent with compact jet disruption and the launching of ejecta (J. C. A. Miller-Jones et al. 2023a). Subsequent X-ray observations, noting variability in the hardness ratio, were suggestive of multiple returns to the intermediate states (e.g., W. Yu 2023). Swift J1727 took \sim 6 months to transition back to the hard state, and by that time its X-ray luminosity decreased by more than 2 orders of magnitude (on 2024 March 15, \sim MJD 60385; J. Podgorny et al. 2024; T. D. Russell et al. 2024). Swift J1727 has since returned to quiescence.

This paper combines observations from multiple collaborations to present a multiwavelength, multifacility radio light curve of Swift J1727 during its 2023-2024 outburst. In addition to flux densities, we include, when available, inter-band radio spectral indices but omit all other properties (e.g., morphology, proper motion, or polarization), as the comprising collaborations have identified them as the focus of in preparation publications. Our goal is to provide the broader community with comprehensive radio light curves to aid with interpreting the evolution of Swift J1727, particularly for observing programs at other wavelengths (e.g., X-ray or optical monitoring). The rest of the paper is structured as follows: Section 2 describes the observing and analysis strategies for each instrument; Section 3 presents the light curves and a qualitatively focused interpretation of the source evolution; and finally, Section 4 presents a summary of the observations.

2. Data and Analysis

This section summarizes each instrument's data reduction, calibration, imaging, and analysis techniques. We focus on concise summaries as the collaborations will publish standalone papers with more comprehensive descriptions of their observation and analysis routine(s). In Figure 1, we include a graphical representation of the radio coverage.

2.1. MeerKAT

Swift J1727 was observed with the radio interferometer MeerKAT (J. Jonas & MeerKAT Team 2016) as a part of the ThunderKAT (R. Fender et al. 2016) and X-KAT programs (MeerKAT Proposal ID: SCI-20230907-RF-01). MeerKAT is a 64-element interferometer with a maximum baseline length of 8 km. The MeerKAT monitoring includes 52 epochs taken on an approximately weekly observing cadence. Most observations (i.e., 47 epochs) used the L-band receivers (\sim 1.28 GHz; 856 MHz unflagged bandwidth). Each L-band observation consisted of a single scan of either 15 or 30 minutes on-source, flanked by two 2 minute scans of a nearby gain calibrator (J1733-1304). Two 5 minute scans of J1939-6342 (PKS B1934-638) were included at the beginning and end of each observation for bandpass and flux scale calibration. In addition to the weekly L-band monitoring, five epochs were acquired using MeerKAT's S-band receivers. One of the S-band observations used the S2 (~2.62 GHz; 875 MHz unflagged bandwidth) subband, and the other four used the S4 (~3.06 GHz; 875 MHz unflagged bandwidth) subband. The S-band monitoring followed the L-band observing strategy.

The data were flagged, calibrated, and imaged using POLKAT (A. K. Hughes et al. 2025),³⁴ which is based on the semiautomated routine OXKAT (I. Heywood 2020), but modified to handle full polarization observations. This work

³⁴ https://github.com/AKHughes1994/polkat

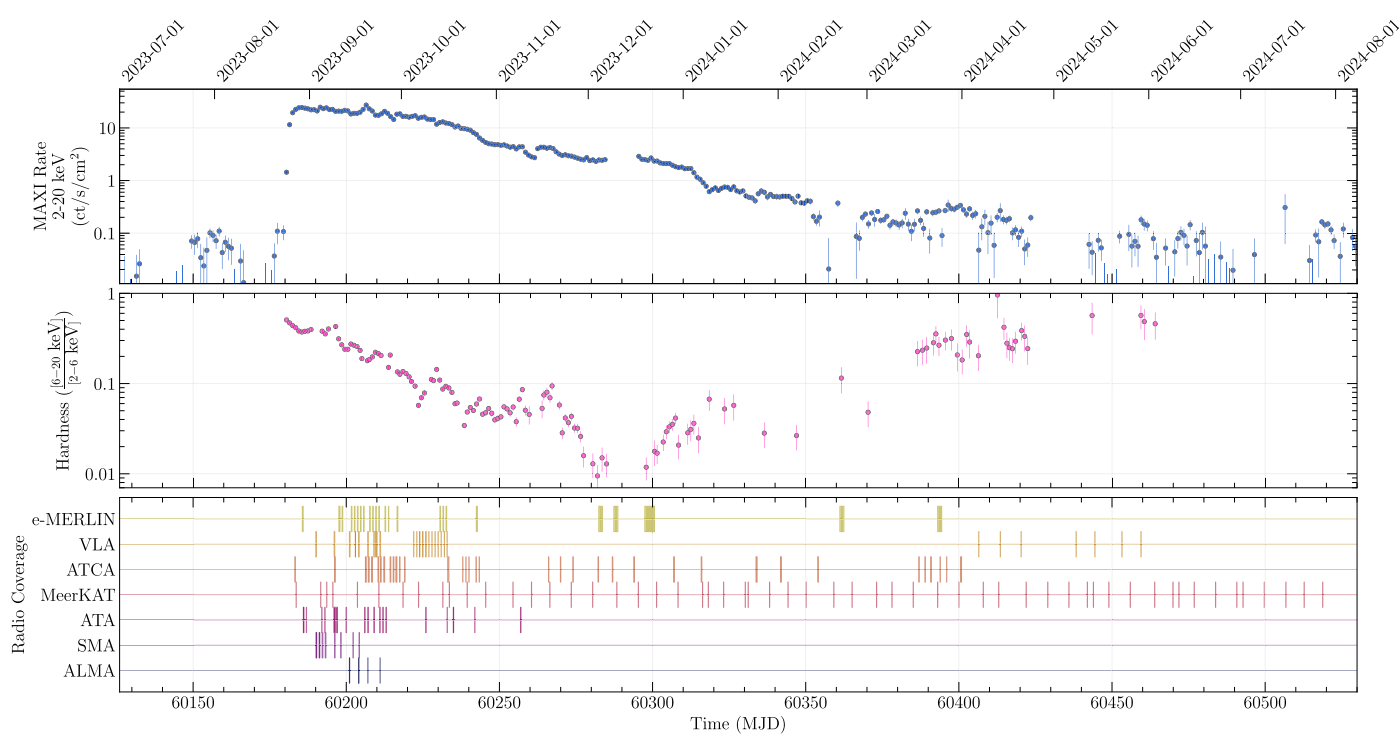


Figure 1. Representation of the radio coverage during the 2023–2024 monitoring campaign of Swift J1727. Top panel: the MAXI/GSC 2–20 keV rate. Middle panel: the hardness ratio calculated using the 2–6 keV and 6–20 keV subbands. Bottom panel: the coverage from each radio facility. When calculating the hardness ratio, we average together adjacent observations until both bands are detected at 3σ ; as a result, the top and middle panels have different time samplings. In the bottom panel, each instrument is represented by a different color, and the width of each line is the duration of each observation.

only includes total intensity observations (i.e., Stokes *I*), and thus, OXKAT and POLKAT have near-identical workflows. Readers are directed to I. Heywood et al. (2022) for a comprehensive description of the workflow, but should note that calibration stopped after the direction-independent self-calibration step (2GC in OXKAT parlance). To optimize for high-sensitivity imaging, the image weighting adopted a Briggs' robustness of 0 (D. S. Briggs 1995).³⁵

The source properties were measured using the Common Astronomy Software Applications package (CASA, v6.4; CASA Team et al. 2022) task IMFIT, fitting elliptical Gaussian component(s) in a small subregion around the source.

Multiple Gaussians were simultaneously fit for observations with multiple components (e.g., due to jet ejecta). As the components were unresolved point sources, the component shapes were fixed to the synthesized beam of each image. The (1σ) uncertainty on the flux densities was measured from the local rms noise extracted from an emission-free region centered near the source(s); the extraction region had an area equal to ~ 100 point-spread functions. No further data manipulation was applied.

2.2. Enhanced Multi-element Remote-linked Interferometer Network

Swift J1727 was also monitored with the Enhanced Multielement Remote-linked Interferometer Network (e-MERLIN) radio interferometer (S. Garrington & R. Beswick 2016) for 24 epochs in total, from 2023 August to 2024 March (Project Codes RR16003 and CY16208). e-MERLIN is a seven-antenna array with a maximum baseline of $217 \,\mathrm{km}$. The first part of the monitoring consisted of a dense coverage at the beginning of the outburst, with 19 observations performed almost daily in 2024 September and during the second half of 2024 October, with durations that ranged from 1 to 5.5 hr per epoch, depending on the expected flux density of the target. In this period, observations were performed at the C band, with a central frequency of 5.07 GHz and a total bandwidth of 512 MHz.

The second part of the monitoring started on 2023 December 4 (MJD 60283) and ended on 2024 March 24 (MJD 60393), with five observations log-spaced in time and durations of up to $10 \, \text{hr}$. In this part of the campaign, observations were performed at the L band, at a central frequency of $1.51 \, \text{GHz}$ and a total bandwidth of $512 \, \text{MHz}$.

For the entire campaign, 3C286 and OQ208 were observed as the flux and bandpass calibrators, respectively, while J1724–1443 was used as the gain calibrator. The data were processed using the e-MERLIN CASA Pipeline (J. Moldon 2018), v1.1.19.³⁶ The pipeline handles the automated a priori flagging with AOFLAGGER (A. R. Offringa 2010) and the standard bandpass and gain calibration using CASA. For each epoch, since it was intended to build a homogeneous light curve from epochs with very different samplings of the *u*–*v* plane, the flux density of Swift J1727 was extracted through visibility-plane fitting using UVMULTIFIT (assuming a point source; I. Martí-Vidal et al. 2014).

2.3. Allen Telescope Array

Observations of Swift J1727 with the Allen Telescope Array (ATA; J. S. Bright et al. 2023; A. Pollack et al. 2025, in

 $[\]overline{^{35}}$ MeerKAT's synthesized beam becomes non-Gaussian for robustness weightings that would typically be used when maximizing for sensitivity (i.e., >0); non-Gaussian beam shapes can inhibit accurate deconvolution, thereby raising the image-plane noise.

³⁶ https://github.com/e-MERLIN/eMERLIN_CASA_pipeline

preparation; W. Farah et al. 2025, in preparation) began on 2023 August 30 with regular monitoring occurring until 2023 November 8. These observations used 20 (out of 42) of the ATA antennas and had a maximum baseline length of 300 m. The ATA is equipped with wide-bandwidth feeds, sensitive to frequencies between ~ 1 and ~ 10 GHz. The current digitization capabilities of the ATA backend allow for two \sim 700 MHz bandwidth tunings to be placed independently within this frequency range. The observing campaign included data at central frequencies of 1.5, 3, 5, and 8 GHz. The flux/bandpass and gain calibrators were 3C286 and J1733-1304, respectively. The gain calibrator was visited every 30 minutes at all frequencies. Following the standard procedures, data were reduced in CASA; imaging was performed using WSCLEAN; the flux density of Swift J1727 was measured following Section 2.1.

2.4. Karl G. Jansky Very Large Array

This work includes three separate observing programs with the Very Large Array (VLA). We combine data taken in multiple VLA configurations, and as a result, the 27-antenna array has a (program-dependent) maximum baseline of 3–36 km. When available, we also include ~0.3 GHz flux densities taken with the VLA Low-band Ionosphere and Transient Experiment (VLITE; e.g., W. M. Peters et al. 2023). VLITE is a commensal instrument on the VLA operated by the U.S. Naval Research Laboratory; a description of the VLITE processing pipeline can be found in E. Polisensky et al. (2016).

The most rapid-response observations presented in this work were taken on 2023 August 25 (MJD 60181; J. C. A. Miller-Jones et al. 2023b) as a part of the JACPOT program (Project Code: VLA/23A-260). Initially approved for rapid-response C-band (4–8 GHz) observations, JACPOT also monitored the source daily at the C and X bands (8–12 GHz) during the bright flaring seen in October 2023. The rapid-response observations were taken using the array's most extended A configuration, whereas the flaring occurred when the source was in a hybrid configuration (A \rightarrow D). Each JACPOT observation was 20–30 minutes long and used the VLA's 8-bit samplers, which break each band into two basebands with 1.024 GHz of bandwidth.

Additionally, during the rising hard state of the outburst, Swift J1727 was also observed by the PITCH-BLACK collaboration (Project Code: VLA/22B-069). The multi-hour PITCH-BLACK observations split the 27-element array (in A configuration) into three subarrays of ten, nine, and eight antennas. Observations in each subarray were also made with the 8-bit samplers, and each subarray was observed exclusively in one frequency band: C (4–8 GHz), X (8–12 GHz), or Ku (12–14 GHz) band.

Following the source's return to the hard state, the VLA observed Swift J1727 nine additional times on an approximately weekly cadence (Project Code: VLA/23B-064). Observation durations ranged from 10 to 60 minutes, where longer epochs were taken as the source faded. Observations were recorded at the *C* band with 3-bit samplers, resulting in 4.096 GHz of bandwidth centered at 6.2 GHz. The epochs of this final VLA program were evenly split between the B and C configurations.

All three VLA projects used 3C286 (J1331+305) for bandpass and flux scale calibration and J1733-1304 for gain calibration. The multi-hour, subarrayed observations (i.e., VLA/22B-069) implemented a custom nonperiodic target/

calibrator cycle for each subarray, alternating between Swift J1727 and the calibrators at one band per subarray, such that simultaneous data in all three bands were obtained. The data were reduced and imaged within CASA, with flagging and calibration performed using the VLA CASA pipeline.³⁷ The images were weighted with natural or robust weighting (robustness parameter 0). When necessary, phase-only self-calibration was used to improve image fidelity. Flux densities were measured by fitting a point source in the image plane, as outlined in Section 2.1.

2.5. Australia Telescope Compact Array

The Australia Telescope Compact Array (ATCA) observed Swift J1727 39 times during its 2023-2024 outburst under Project Codes C2601, C3057, and C3362. ATCA is an eastwest array with six antennas and a maximum baseline length of 6 km. For all observations, data were recorded simultaneously at central frequencies of 5.5 and 9 GHz, with each frequency band having 2.048 GHz of unflagged bandwidth. Observations used either J1939-6342 (PKS B1934-638) or PKS B0823-500 for bandpass and flux density calibration, depending on source visibility at the time of the observation; J1939–6342 was the preferred calibrator. The nearby (\sim 3.4 away) source J1733-1304 (PKS B1730-130) was used for gain calibration. Data were first edited for radio-frequency interference, before being calibrated and imaged following standard procedures within CASA v5.1.2. Imaging typically used a Briggs robustness parameter of 0, balancing sensitivity and resolution. However, at later times, when the source was faint, more natural weightings (robustness parameter >0) were used to increase sensitivity. Data were phase-only selfcalibrated when the source flux density exceeded $\sim 10 \, \mathrm{mJy}$. The flux density of the source was measured following the same procedure as Section 2.1.

2.6. Atacama Large Millimeter/submillimeter Array

Alongside the PITCH-BLACK observations taken with the VLA, Swift J1727 was observed with the Atacama Large Millimeter/submillimeter Array (ALMA; Project Code: 2022.1.01182.T) four times in 2023 September. Data were taken in Band 3, Band 4, and Band 6 at central frequencies of 97.5 GHz, 145.0 GHz, and 233 GHz, respectively. The ALMA correlator was set up to yield 4×2 GHz-wide basebands. During the observations, the array was in its Cycle 10 C8 configuration, with 42-46 antennas and a maximum baseline length of 8.5 km. The data were reduced and imaged within CASA, with flagging and calibration performed using the ALMA CASA v6.2 pipeline. J1924–2914 was used as a flux/ bandpass calibrator, J1733-1304 was used as a phase calibrator, and J1742-1517 was used as a check source in all bands. Phase-only self-calibration was performed, and imaging followed standard procedures with a natural weighting scheme to maximize sensitivity. Flux densities of the source were then measured by fitting a point source in the image plane (with the IMFIT task).

³⁷ The VLA programs used CASA v6.2, 6.2, and 6.3 for Project Codes VLA/23A-260, VLA/22B-069, and VLA/23B-064, respectively.

2.7. Submillimeter Array

Swift J1727 was observed with the Submillimeter Array (SMA) eight times in 2023 September. The SMA correlator yields 12 GHz of bandwidth per sideband per polarization and was tuned to a frequency of 225.5 GHz. During the observations, the array was in the subcompact configuration, with seven available antennas and a maximum baseline length of 25 m. The data were reduced and imaged with multiple reduction paths using in-house pipeline routines, the in-house reduction suite MIR,³⁸ and MIRIAD (R. J. Sault et al. 1995), assuring a consistent outcome. The flux density scale was set using MWC349A, BL Lac was the bandpass calibrator, and NRAO 530 (J1733–1304) was used as the gain calibrator. The target is a point source at the spatial resolution of the SMA during the observations (~5"), and source properties were extracted through visibility-plane fitting.

3. Results and Discussion

This section presents the radio observations of the 2023-2024 outburst of Swift J1727. To highlight the simultaneous X-ray evolution, we include a X-ray hardness-intensity diagram (HID) using publicly available data from the Monitor of All sky X-ray Image Gas Slit Camera (MAXI/GSC; M. Matsuoka et al. 2009; T. Mihara et al. 2011). The HID is presented in Figure 2, where the arrows show the time evolution of the source and the marker colors trace the radio flux density (scaled to 10 GHz following the routine discussed in Section 3.1.1). The green diamond and yellow star correspond to the reported hard-to-soft (N. Bollemeijer et al. 2023a, 2023b) and soft-to-hard (J. Podgorny et al. 2024) state transitions, respectively. The increase in the hardness ratio following the (initial) reporting of a hard-to-soft state transition is consistent with the reporting by W. Yu (2023) that stated the source returned to the hard state; as a result, Swift J1727 almost certainly underwent multiple hard-to-soft state transitions. From the HID, it is clear that Swift J1727 completed the canonical loop (or "turtle head") pattern seen from BH LMXB outbursts (e.g., R. P. Fender et al. 2004; T. M. Belloni 2010), before fading below detectability, and likely returning to quiescence.

The remainder of this section focuses on the evolution of the flux densities and spectral indices from the jet. We only report statistical errors, but we note that telescopes have (frequency-dependent) systematic errors due to uncertainty in the absolute flux scale. Here, we present the integrated radio flux densities; for observations with multiple components (e.g., compact jet and jet ejecta or multiple jet ejecta), we sum the flux densities from the individual components, adding their errors in quadrature as an estimate of the integrated flux density errors. While in some cases this will be summing information from the core and ejecta, which are physically decoupled, it mimics what would be measured with only low-angular-resolution monitoring and still captures much of the critical astrophysics.

Aside from the image weightings mentioned in Section 2, we do not apply any further manipulation of the visibilities during imaging (e.g., no *uv* tapering). Care should be taken when combining data from different telescopes as they will probe different angular scales, and as a result, may resolve some flux density (this is primarily an issue for jet ejecta and when comparing e-MERLIN to the other non-very-long-baseline interferometry facilities). Regarding the radio spectral

The radio properties are graphically represented in Figures 3 and 4. We include per-observatory light curves in Appendix A, and the raw data are presented in Appendix B. The data and plotting scripts are available via GitHub³⁹ and Zenodo (doi:10.5281/zenodo.15389817).

3.1. Radio Outburst of Swift J1727.8-1613

The radio evolution of Swift J1727 is shown in Figure 3 (top panel, light curves; bottom panel, spectral indices). The dashed—dotted and dashed vertical lines correspond to the reported hard-to-soft (2024 October 5, MJD 60222) and soft-to-hard (2024 March 15, MJD 60385) state transitions, respectively (N. Bollemeijer et al. 2023a, 2023b; J. Podgorny et al. 2024).

3.1.1. The Initial Hard State and State Transition(s)

After the onset of the outburst (2023 August 24, MJD 60180), the source exhibited a sharp rise in its radio flux density, reaching $\sim\!100\,\mathrm{mJy}$ at all frequencies due to its flat spectral index (i.e., $\alpha\sim0$), consistent with emission from a partially self-absorbed compact jet. Swift J1727 remained at $\sim100\,\mathrm{mJy}$ for a few weeks before undergoing a decrease in radio flux density, followed by a period of flaring in the lead-up to (and immediately after) the reported hard-to-soft state transition. The radio flaring occurred (approximately) between 2023 September 20 (MJD 60207) and 2023 November 1 (MJD 60249), and the brightest flare reached a flux density of $\sim\!1\,\mathrm{Jy}$ at $\sim\!1.28\,\mathrm{GHz}.$

Figure 4 shows a "zoomed-in" view of the flaring period (gray region, Figure 3). The top panel adopts the same marker style and color scheme as Figure 3. The middle panel presents a monochromatic light curve, where each observation is scaled to 10 GHz using the nearest spectral index measurement. We fold the error in the spectral indexes into our monochromatic flux densities, adopting Gaussian error propagation. However, we note that spectral index variability is an unaccounted-for systematic effect on the scaled flux density of single-frequency observations (i.e., observations where an inter-band spectral index was not calculated). As a result, we exclude observations with central frequencies that have more than an order of magnitude separation from 10 GHz (i.e., <1 GHz or >100 GHz) from the monochromatic light curves, as large frequency separations will be more affected by errors in the adopted spectral indices. Moreover, systematic errors may significantly worsen during flaring when the radio spectral index is frequency dependent and rapidly evolving. Despite the systematics, we include the monochromatic light

indices, we exclusively calculate inter-band values given that intra-band spectral indices have known biases (e.g., as shown in the 1–2 GHz VLA Sloan Digital Sky Survey Stripe 82 survey; I. Heywood et al. 2016). As the source is highly variable, we only calculate these inter-band spectral indices for strictly simultaneous multifrequency observations. By enforcing strict simultaneity, each spectral index is computed using flux densities from a single observatory (ATCA, VLA, or ATA), thereby avoiding complications arising from differences in angular scale sensitivity across telescopes. Moreover, the multifrequency observations at these facilities are sensitive to angular scales much larger than the typical source size (≲1″), mitigating the risk of artificial spectral features caused by frequency-dependent spatial filtering.

³⁸ https://lweb.cfa.harvard.edu/rtdc/SMAdata/process/mir/

https://github.com/AKHughes1994/SwJ1727_2023_Outburst

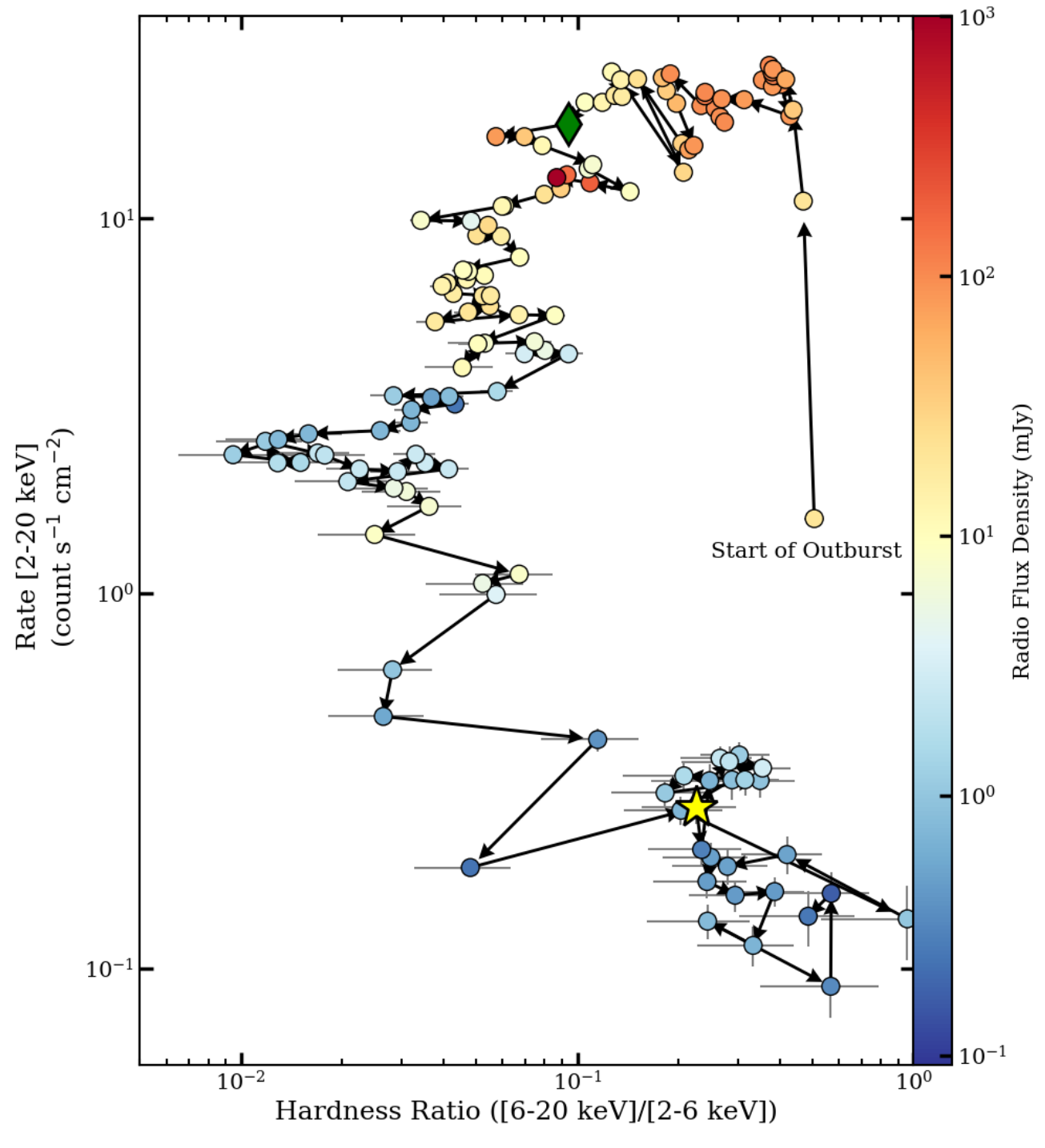


Figure 2. X-ray hardness—intensity diagram (HID) of Swift J1727 when it was detectable by MAXI/GSC. The marker colors correspond to the scaled 10 GHz radio flux densities, linearly interpolated (in time) to the MAXI/GSC observing epochs. The color bar has been capped at 1 Jy to show the radio evolution more clearly. We highlight the observations where the source was first identified to undergo a hard-to-soft (green diamond, MJD 60222; N. Bollemeijer et al. 2023a, 2023b) and a soft-to-hard (yellow star, MJD 60385; J. Podgorny et al. 2024) state transition. From the HID, it is clear that Swift J1727 has completed the "loop," marking the end of the source's X-ray activity.

curves as a qualitative description of the flaring progression, and we caution readers to view it as such.

Both the poly- and monochromatic light curves clearly show multiple radio flares consistent with the reporting from W. Yu (2023) that Swift J1727 underwent multiple hard-to-soft state transitions. The two most pronounced flares peaked at $\sim\!300\,\mathrm{mJy}$ (0.338 GHz; MJD 60223) and $\sim\!800\,\mathrm{mJy}$ (1.28 GHz; MJD 60231). Alongside the flaring, the radio spectral indices varied

between $\alpha \sim 0.9$ and $\alpha \sim -1.5$, on timescales as short as days. Simultaneous flux density and spectral evolution are typical of the flaring associated with the launching of jet ejecta (e.g., R. Fender & J. Bright 2019), and a decrease in flux density in the lead-up to flaring (attributed to compact jet quenching) has been observed in other BH LMXBs (e.g., C. Brocksopp et al. 2002; T. D. Russell et al. 2019). Recently, the launching of jet ejecta during flaring has been confirmed via direct imaging (C. M. Wood et al. 2025).

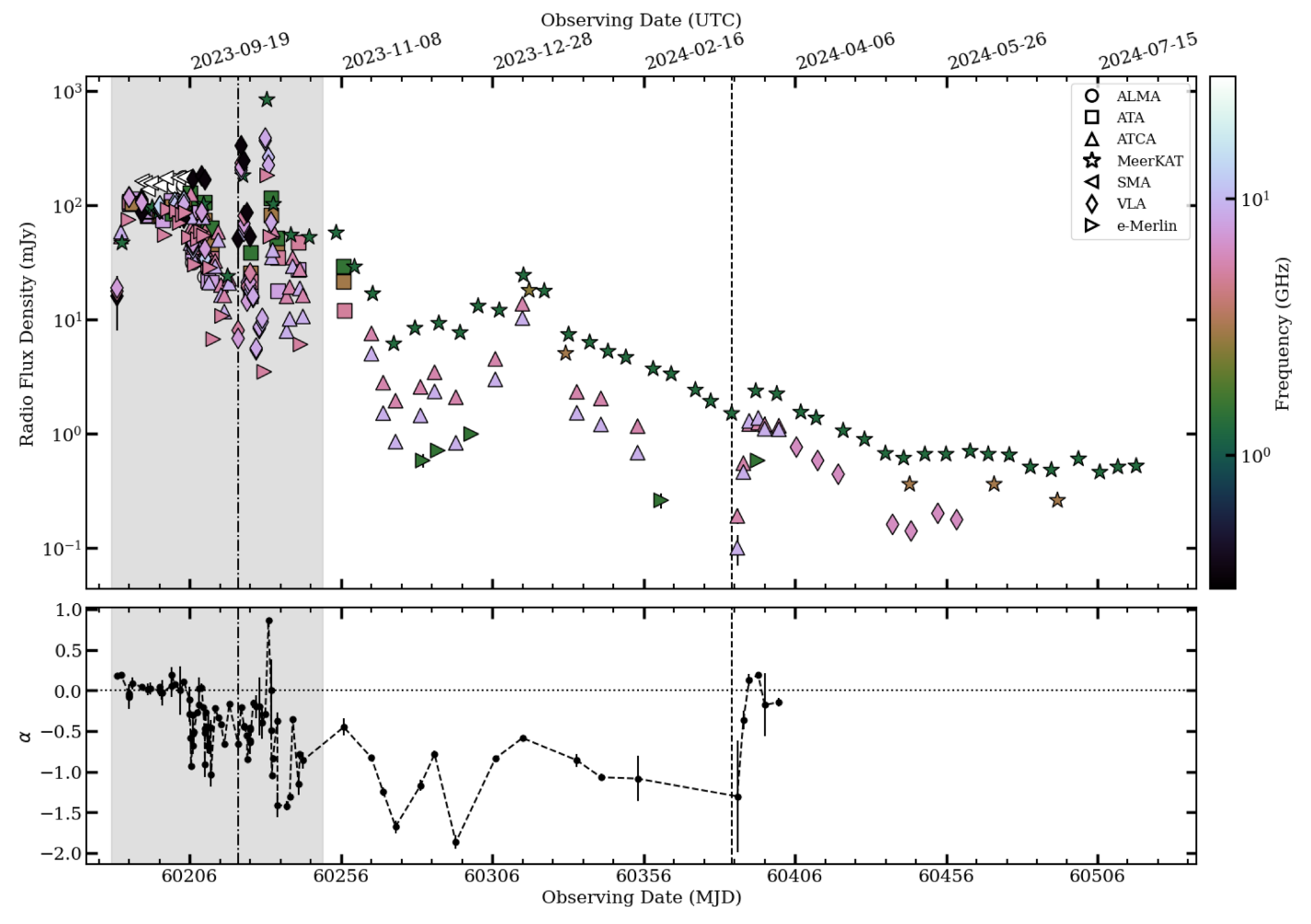


Figure 3. The full radio light curves of Swift J1727.8–1613 during its 2023–2024 outburst. Top panel: the integrated flux density evolution. Each marker corresponds to a different telescope, and the marker colors correspond to the observing frequency. To ease visualization, we have saturated the color axis at 30 GHz; the saturation only affects observations taken with ALMA or the SMA. Bottom panel: the inter-band spectral index evolution. The dashed–dotted and dashed lines correspond to the hard-to-soft (2024 October 5, MJD 60222) and soft-to-hard (2024 March 15, MJD 60385) state transitions, respectively. The gray shaded region highlights the period of bright radio flaring that is shown in Figure 4.

Following the prescription from R. Fender & J. Bright (2019), assuming equipartition of energy between particles and magnetic fields, and adopting distances of 3.7-5.5 kpc (B. J. Burridge et al. 2025; D. Mata Sánchez et al. 2025), we can estimate the minimum internal energy (E_{min}) required to produce each flare. The observed flaring corresponds to an $E_{\rm min} \sim (0.6-2) \times 10^{40}$ erg, consistent with the range of energies inferred from other sources (albeit at the higher end; R. Fender & J. Bright 2019; T. D. Russell et al. 2019; J. S. Bright et al. 2020; F. Carotenuto et al. 2021). It should be noted that alternative and perhaps more robust methods of minimum-energy estimation regularly arrive at values orders of magnitude higher than those inferred from flaring alone (e.g., kinematic modeling or direct size measurements of ejecta; J. S. Bright et al. 2020; F. Carotenuto et al. 2022, 2024). As a result, these estimates are likely a conservative minimum.

3.1.2. The Soft State

Following the flaring, Swift J1727 transitioned to the soft state, where its flux density began decreasing, reaching $<10\,\mathrm{mJy}$ at all observing frequencies. Swift J1727 then underwent a modest rebrightening that peaked around 2024 January 14 (MJD 60322; $\sim30\,\mathrm{mJy}$ at 1.28 GHz), followed by a

continuation of the flux density decay. Throughout the soft state, the radio spectral index was optically thin, $\alpha\lesssim-0.5$, consistent with the radio emission originating from jet ejecta, which is unsurprising as radio flaring is a known signature of jet ejection events (e.g., R. M. Hjellming & M. P. Rupen 1995; R. P. Fender et al. 1999; A. P. Rushton et al. 2017; J. C. A. Miller-Jones et al. 2019; J. S. Bright et al. 2020; F. Carotenuto et al. 2021) and compact jet emission is heavily quenched in the soft state (e.g., R. Fender et al. 1999; M. Coriat et al. 2011; T. D. Russell et al. 2019, 2020; T. J. Maccarone et al. 2020; F. Carotenuto et al. 2021).

Interestingly, while optically thin, the spectral index was highly variable ($-2\lesssim\alpha\lesssim-0.5$), suggesting a significant evolution in the population of synchrotron emitting particles (likely electrons). The temporal evolution of the spectral index in the soft state is suggestive of particle (re)acceleration, possibly due to jet–ISM interactions (e.g., the longest-lasting ejecta are thought to be driven to continued particle acceleration from jet–ISM interactions; S. Corbel et al. 2002; T. D. Russell et al. 2019; J. S. Bright et al. 2020; F. Carotenuto et al. 2021; A. Bahramian et al. 2023). Indeed, the archetypal long-lived ejecta from XTE J1550–564 showed a similar transition from $\alpha\sim-1.2$ to $\alpha\sim-0.4$, which was interpreted

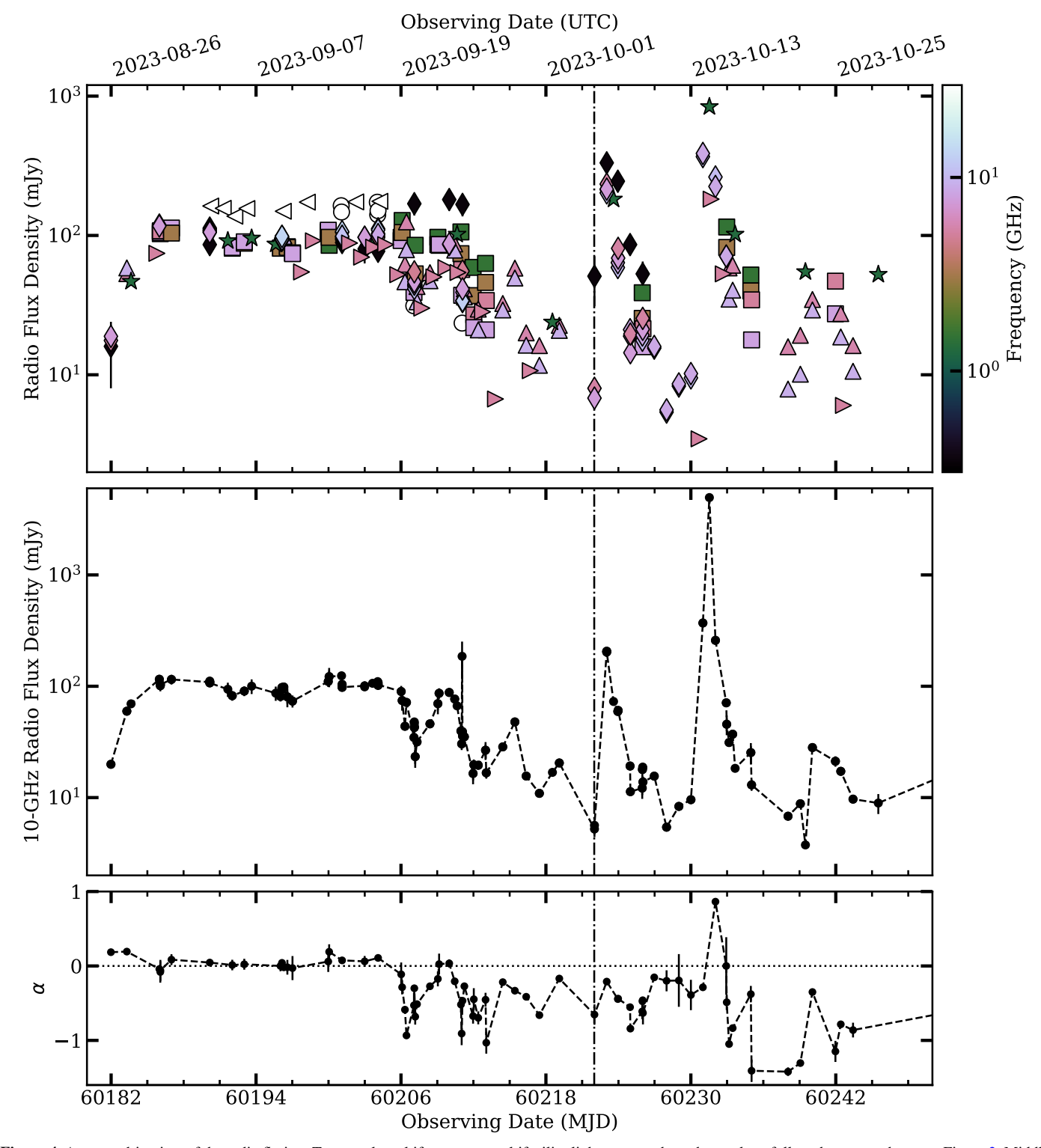


Figure 4. A zoomed-in view of the radio flaring. Top panel: multifrequency, multifacility light curves where the markers follow the same scheme as Figure 3. Middle panel: monochromatic radio light curves, where each of the measured flux densities have been scaled to 10 GHz, adopting the closest (in time) spectral index measurement (excluding high-frequency SMA and ALMA data). Bottom panel: the inter-band spectral indices. The source exhibited multiple bright radio flares, suggesting multiple jet ejection events.

as an interaction-driven renewal of particle acceleration (G. Migliori et al. 2017).

For power-law distributed population synchrotron emitting electrons, $N(E) dE \propto E^{-p} dE$, an optically thin spectral index (α) is related to the power-law index p through $\alpha = -(p-1)/2$. Therefore, for typical values of $p \sim 2$ –3 (M. S. Longair 2011),

optically thin synchrotron emission should have a spectral index between -0.5 and -1. Synchrotron cooling can result in more steep-spectrum emission as $\alpha=-p/2$; however, spectral indexes of $\alpha<-1.5$ still require values of p>3 (e.g., the minimum of $\alpha=-1.86\pm0.08$ on MJD 60293). The origin of steep-spectrum radio sources remains an open question. Prior studies have

suggested thermal (or quasi-thermal) particle distributions (A. G. Pacholczyk & J. A. Roberts 1971), ultrarelativistic shocks (K. R. Ballard & A. F. Heavens 1992), or energy exchange between the particles and turbulent magnetic fields (A. R. Bell et al. 2019) can produce steep spectra. However, most BH LMXBs showing comparably steep spectral indices (i.e., $\alpha \lesssim -1.5$; D. M. Russell et al. 2010; T. Shahbaz et al. 2013) have typically been seen with IR–optical observations of compact jets. Seeing such steep spectral indices for radio observations of ejecta provides an interesting case study for understanding particle acceleration from BH LMXB jets, especially through comparisons with steep-spectrum active galactic nuclei (e.g., K. I. I. Koljonen et al. 2015).

3.1.3. The Final Hard State and the Return to Ouiescence

Toward the end of the outburst, the radio emission of Swift J1727 rebrightened once more after returning to the hard state on (approximately) 2024 March 15 (~MJD 60385; J. Podgorny et al. 2024). For example, ATCA detected an increase from \sim 0.1 mJy to \sim 1 mJy in both its 5.5 and 9.0 GHz bands during observations taken within 4 days, consistent with a reformation of the compact jet (e.g., T. D. Russell et al. 2014). The spectral index evolved from -0.5 to ~ 0 , where the latter value is typical of a partially self-absorbed synchrotron radiation. The emission associated with the compact jet quickly decayed as the source returned to quiescence. Despite returning to X-ray quiescence, the radio emission plateaued due to long-lasting jet ejecta, presumably interacting with the ISM. Jet ejecta are typically optically thin, consistent with our observations having lower flux densities at higher frequencies. The slow decay from ejecta interactions, and as a result, renewed particle acceleration, make Swift J1727 an ideal candidate for investigating jet-based feedback.

4. Conclusion

We have presented a comprehensive multifrequency, multifacility radio monitoring campaign of the BH LMXB Swift J1727 during its 2023-2024 outburst. The presented monitoring period began on 2023 August 25 (MJD 60181) and ended 2024 July 27 (MJD 60518), and includes 198 individual epochs with observing frequencies ranging between 0.3 and 225 GHz, making Swift J1727 one of the most intensely monitored LMXBs to date. Our observations captured the complete outburst evolution, including both the hard-to-soft and soft-to-hard state transitions (i.e., the disruption and reformation of the compact jet), and as a result bright radio flares and spectral index variability. The primary motivation behind this work was to provide the community with comprehensive radio light curves; as a result, we only briefly (and qualitatively) interpreted the data, leaving more comprehensive targeted analyses for future publications by the comprising collaborations. We intend to continue rapidly releasing radio light curves following the cessation of future BH LMXB outbursts, as the radio properties will assist the interpretations drawn from monitoring programs at other wavelengths, akin to how the publicly available MAXI/GSC data are commonly used to interpret the X-ray and accretion state evolution for radio-centered analyses. We encourage other studies of this source to use these data where appropriate.

Acknowledgments

A.K.H. thanks UK Research and Innovation (UKRI) for support. A.J.T. and E.L. acknowledge that this research was undertaken thanks to funding from the Canada Research Chairs Program and the support of the Natural Sciences and Engineering Research Council of Canada (NSERC; funding reference number RGPIN-2024-04458). F.C. acknowledges support from the Royal Society through the Newton International Fellowship program (NIF/R1/211296). T.D.R. is an INAF IAF fellow. R.S. acknowledges INAF grant No. 1.05.23.04.04. J.v.d.E. acknowledges a Warwick Astrophysics prize post-doctoral fellowship made possible thanks to a generous philanthropic donation, and was supported by funding from the European Union's Horizon Europe research and innovation program under the Marie Sklodowska-Curie grant agreement No. 101148693 (MeerSHOCKS) for part of this work. C.M.W. acknowledges financial support from the Forrest Research Foundation Scholarship, the Jean-Pierre Macquart Scholarship, and the Australian Government Research Training Program Scholarship. This project has received funding from the European Research Council (ERC) under the European Union's Horizon 2020 research and innovation program (grant agreement No. 101002352, PI: M. Linares). G.R.S. is supported by NSERC Discovery Grant RGPIN-2021-0400.

This paper makes use of the following ALMA data: ADS/ JAO.ALMA#2022.1.01182.T. ALMA is a partnership of ESO (representing its member states), NSF (USA) and NINS (Japan), together with NRC (Canada), MOST and ASIAA (Taiwan), and KASI (Republic of Korea), in cooperation with the Republic of Chile. The Joint ALMA Observatory is operated by ESO, AUI/NRAO, and NAOJ. The National Radio Astronomy Observatory is a facility of the National Science Foundation operated under cooperative agreement by Associated Universities, Inc. The Submillimeter Array is a joint project between the Smithsonian Astrophysical Observatory and the Academia Sinica Institute of Astronomy and Astrophysics and is funded by the Smithsonian Institution and the Academia Sinica. We recognize that Maunakea is a culturally important site for the indigenous Hawaiian people; we are privileged to study the cosmos from its summit. The MeerKAT telescope is operated by the South African Radio Astronomy Observatory, which is a facility of the National Research Foundation, an agency of the Department of Science and Innovation. We acknowledge the use of the Inter-University Institute for Data Intensive Astronomy (IDIA) data-intensive research cloud for data processing. IDIA is a South African university partnership involving the University of Cape Town, the University of Pretoria, and the University of the Western Cape. The Australia Telescope Compact Array is part of the Australia Telescope National Facility, which is funded by the Australian Government for operation as a National Facility managed by CSIRO. We acknowledge the Gomeroi people as the traditional owners of the ATCA observatory site. e-MERLIN is a National Facility operated by the University of Manchester at Jodrell Bank Observatory on behalf of STFC, part of UKRI. This research has made use of MAXI data provided by RIKEN, JAXA, and the MAXI team.

Appendix A Additional Figures

Figures 5, 6, and 7 show per-observatory light curves.

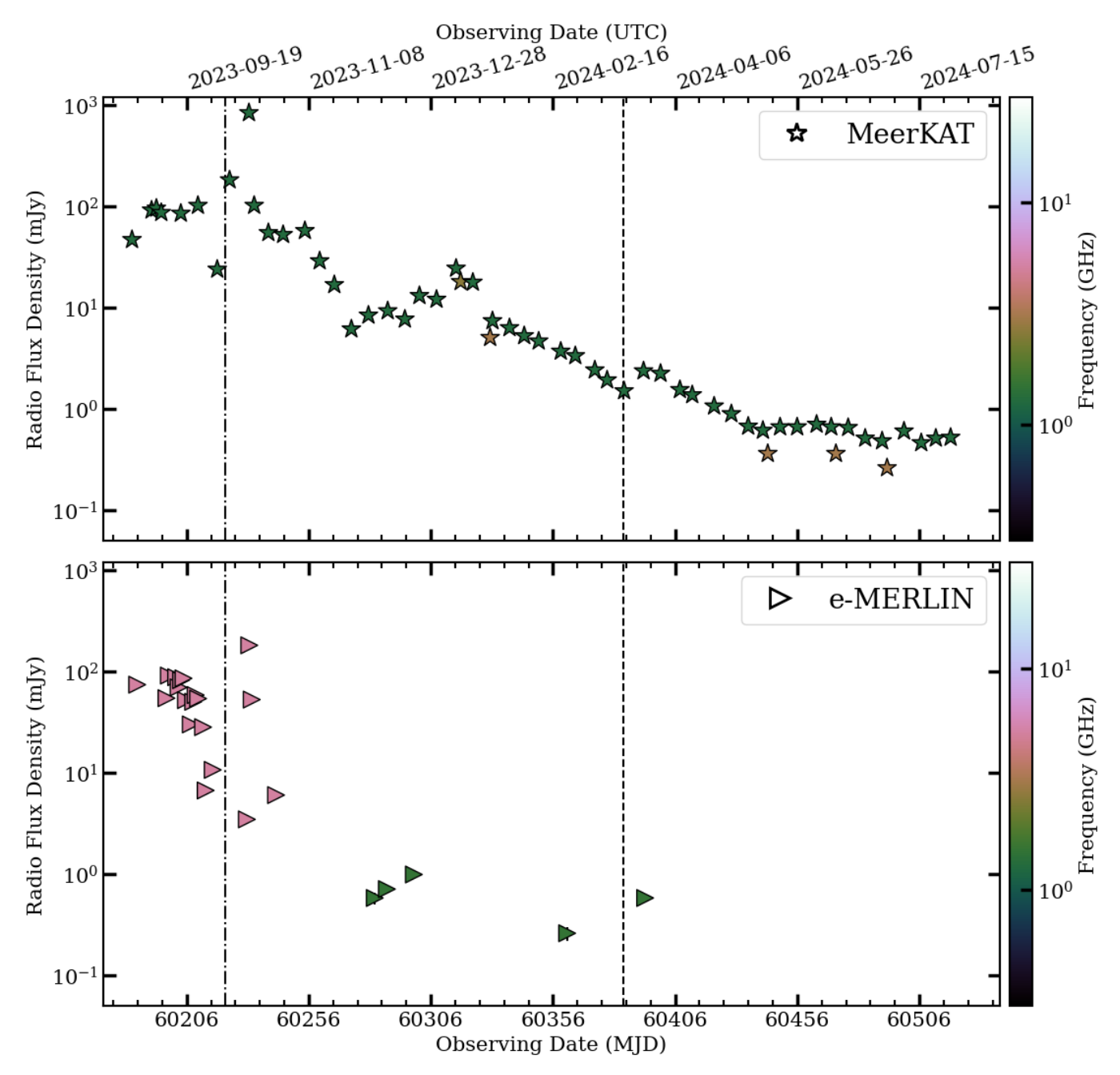


Figure 5. Radio light curves as seen by MeerKAT (top panel) and e-MERLIN (bottom panel). As in Figure 3, the marker colors highlight the observing frequencies and the vertical lines mark the state transitions.

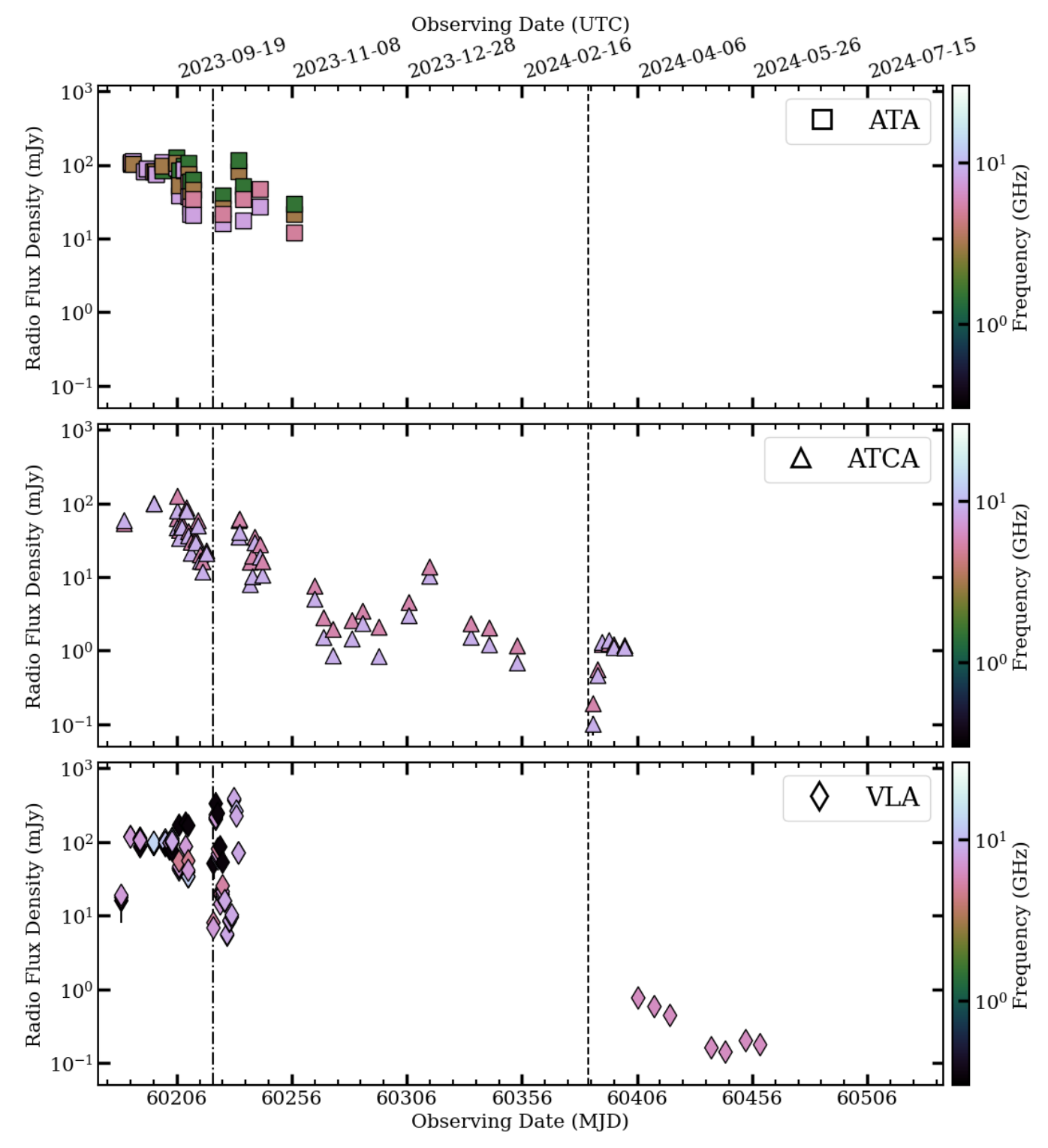


Figure 6. Same as Figure 5 but for ATA (top panel), ATCA (middle panel), and the VLA (bottom panel).

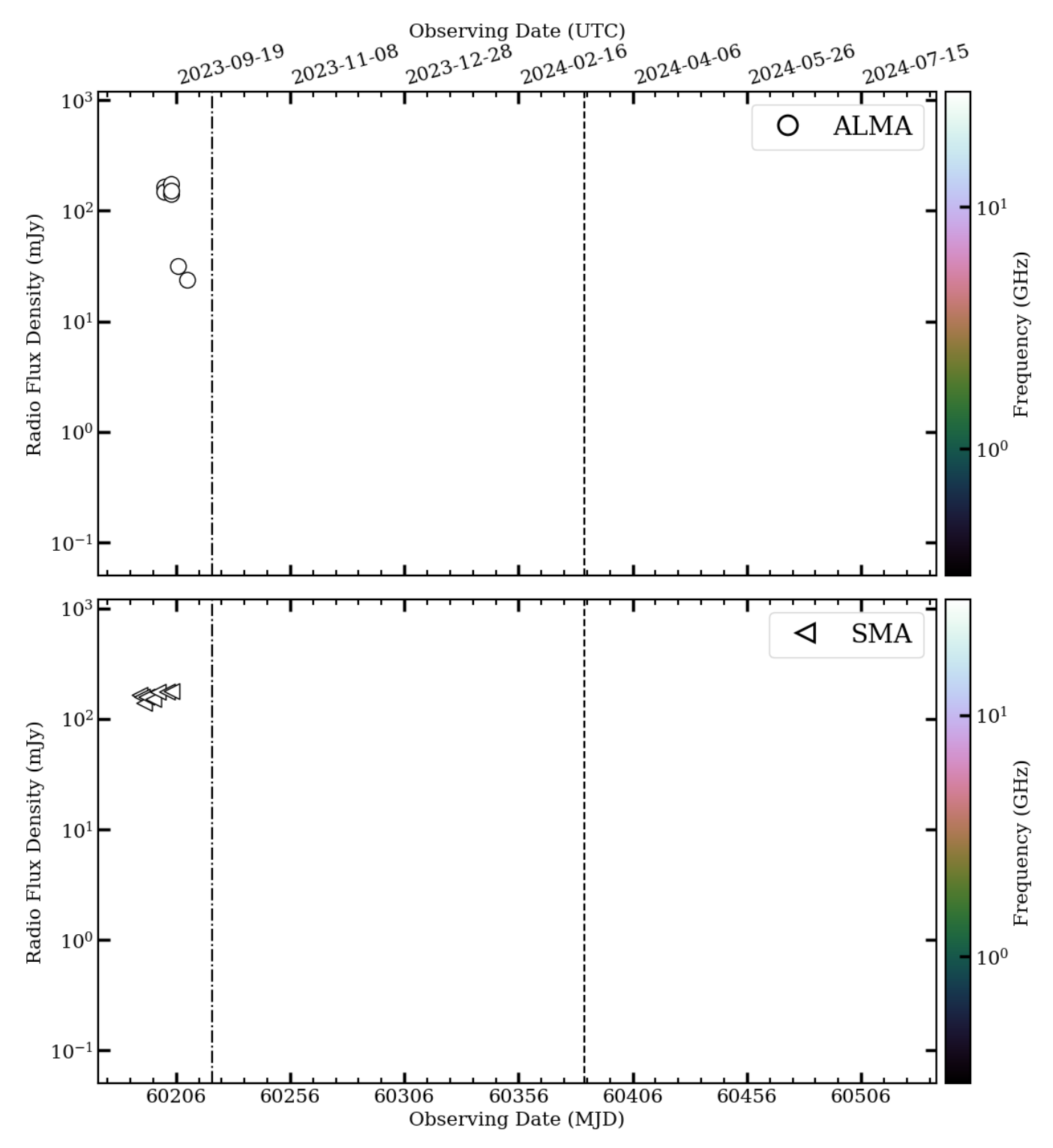


Figure 7. Same as Figure 5 but for ALMA (top panel) and the SMA (bottom panel).

Appendix B Data Tables

Table 1 contains the radio flux densities and observing parameters (e.g., central frequency, duration, and observing date) for each epoch.

 Table 1

 Each Epoch's Observation and Flux Density Information

t _{mid} (UTC)	$t_{ m mid} \ m (MJD)$	Δt (min)	Telescope	$ u_{\rm ctr} $ (GHz)	$F_{ u}$ (mJy)	PI Name	Project ID
2023-08-25 23:35:48	60181.9832	20	VLA	0.338	16 ± 8	Miller-Jones	VLITE/23A-260
2023-08-25 23:35:48	60181.9832	20	VLA	5.2	17.64 ± 0.03	Miller-Jones	23A-260
2023-08-25 23:35:48	60181.9832	20	VLA	7.5	18.88 ± 0.04	Miller-Jones	23A-260
2023-08-27 07:13:43	60183.3012	210	ATCA	5.5	$53.2 ~\pm~ 0.7$	Russell/Carotenuto	C2601/C3057/C3362/CX550
2023-08-27 07:13:43	60183.3012	210	ATCA	9.0	$58.5 ~\pm~ 0.3$	Russell/Carotenuto	C2601/C3057/C3362/CX550
2023-08-27 15:35:25	60183.6496	15	MeerKAT	1.28	46.77 ± 0.03	Fender	X-KAT/ThunderKAT
2023-08-29 18:59:02	60185.791	265	e-MERLIN	5.07	74.4 ± 0.1	Williams-Baldwin/Carotenuto	RR16003
2023-08-29 23:49:29	60185.9927	20	VLA	5.2	118.73 ± 0.03	Miller-Jones	23A-260
2023-08-29 23:49:29	60185.9927	20	VLA	7.5	116.93 ± 0.04	Miller-Jones	23A-260
2023-08-30 01:43:49	60186.0721	176	ATA	8.0	103 ± 5	Bright	•••
2023-08-30 01:43:49	60186.0721	176	ATA	5.0	107 ± 5	Bright	•••
2023-08-30 01:54:54	60186.0798	154	ATA	8.0	105 ± 5	Bright	•••
2023-08-30 01:54:54	60186.0798	154	ATA	5.0	108 ± 5	Bright	•••
2023-08-30 23:53:31	60186.9955	63	ATA	8.0	113 ± 6	Bright	•••
2023-08-30 23:53:31	60186.9955	63	ATA	3.0	104 ± 5	Bright	•••
2023-09-03 03:59:36	60190.1664	210	VLA	4.75	105.21 ± 0.07	Tetarenko	22B-069
2023-09-03 03:59:36	60190.1664	210	VLA	0.338	86 ± 13	Tetarenko	VLITE/22B-069
2023-09-03 03:59:36	60190.1664	210	VLA	8.5	108.39 ± 0.08	Tetarenko	22B-069
2023-09-03 03:59:36	60190.1664	210	VLA	13.5	112.9 ± 0.2	Tetarenko	22B-069
2023-09-03 03:59:36	60190.1664	210	VLA	12.5	111.0 ± 0.2	Tetarenko	22B-069
2023-09-03 03:59:36	60190.1664	210	VLA	11.0	107.92 ± 0.09	Tetarenko	22B-069
2023-09-03 03:59:36	60190.1664	210	VLA	7.5	105.59 ± 0.06	Tetarenko	22B-069
2023-09-03 05:54:48	60190.2464	148	SMA	225.0	162.6 ± 0.4	Vrtilek/Gurwell	2023A-S051
2023-09-04 06:41:19	60191.2787	69	SMA	225.0	156.6 ± 0.5	Vrtilek/Gurwell	2023A-S051
2023-09-04 15:55:43	60191.6637	15	MeerKAT	1.28	91.58 ± 0.04	Fender	X-KAT/ThunderKAT
2023-09-05 00:42:54	60192.0298	104	ATA	3.0	81 ± 4	Bright	•••
2023-09-05 00:42:54	60192.0298	104	ATA	8.0	82 ± 4	Bright	•••
2023-09-05 05:50:38	60192.2435	188	SMA	225.0	$137.5 ~\pm~ 0.5$	Vrtilek/Gurwell	2023A-S025
2023-09-06 00:36:34	60193.0254	145	ATA	3.0	88 ± 4	Bright	•••
2023-09-06 00:36:34	60193.0254	145	ATA	8.0	90 ± 5	Bright	•••
2023-09-06 05:47:11	60193.2411	180	SMA	225.0	156.1 ± 1.4	Vrtilek/Gurwell	2023A-S025

Note. The variables t_{mid} , Δt , ν_{ctr} , and F_{ν} correspond to the midpoint of the observation, approximate observation length, central frequency, and integrated flux density, respectively.

(This table is available in its entirety in machine-readable form in the online article.)

ORCID iDs

Andrew K. Hughes https://orcid.org/0000-0003-0764-0687 Francesco Carotenuto https://orcid.org/0000-0002-0426-3276

Thomas D. Russell https://orcid.org/0000-0002-7930-2276 Alexandra J. Tetarenko https://orcid.org/0000-0003-3906-4354

James C. A. Miller-Jones https://orcid.org/0000-0003-3124-2814

Arash Bahramian https://orcid.org/0000-0003-2506-6041 Joe S. Bright https://orcid.org/0000-0002-7735-5796 Fraser J. Cowie https://orcid.org/0009-0009-0079-2419 Mark A. Gurwell https://orcid.org/0000-0003-0685-3621 Michael McCollough https://orcid.org/0000-0002-8384-3374

Richard M. Plotkin https://orcid.org/0000-0002-7092-0326 Ramprasad Rao https://orcid.org/0000-0002-1407-7944 Saeqa D. Vrtilek https://orcid.org/0000-0002-7521-9897 David R. A. Williams-Baldwin https://orcid.org/0000-0001-7361-0246

Callan M. Wood https://orcid.org/0000-0002-2758-0864 Gregory R. Sivakoff https://orcid.org/0000-0001-6682-916X

Wael Farah https://orcid.org/0000-0002-0161-7243
Poshak Gandhi https://orcid.org/0000-0003-3105-2615
Karri I. I. Koljonen https://orcid.org/0000-0002-9677-1533
James H. Matthews https://orcid.org/0000-0002-3493-7737
Sera B. Markoff https://orcid.org/0000-0001-9564-0876
Alexander W. Pollak https://orcid.org/0000-0002-3430-7671

David M. Russell https://orcid.org/0000-0002-3500-631X Payaswini Saikia https://orcid.org/0000-0002-5319-6620 Noel Castro Segura https://orcid.org/0000-0002-5870-0443 Aarran W. Shaw https://orcid.org/0000-0002-8808-520X Andrew Siemion https://orcid.org/0000-0003-2828-7720 Roberto Soria https://orcid.org/0000-0002-4622-796X John A. Tomsick https://orcid.org/0000-0001-5506-9855 Jakob van den Eijnden https://orcid.org/0000-0002-5686-0611

References

```
Bahramian, A., Tremou, E., Tetarenko, A. J., et al. 2023, ApJL, 948, L7
Ballard, K. R., & Heavens, A. F. 1992, MNRAS, 259, 89
Barthelmy, S. D., Barbier, L. M., Cummings, J. R., et al. 2005, SSRv, 120, 143
Bell, A. R., Matthews, J. H., & Blundell, K. M. 2019, MNRAS, 488, 2466
Belloni, T., Méndez, M., van der Klis, M., Lewin, W. H. G., & Dieters, S.
   1999, ApJL, 519, L159
Belloni, T. M. 2010, in The Jet Paradigm, ed. T. Belloni (Berlin: Springer), 53
Blandford, R. D., & Königl, A. 1979, ApJ, 232, 34
Bollemeijer, N., Uttley, P., Buisson, D., et al. 2023a, ATel, 16247, 1
Bollemeijer, N., Uttley, P., Buisson, D., et al. 2023b, ATel, 16273, 1
Briggs, D. S. 1995, AAS Meeting, 187, 112.02
Bright, J. S., Fender, R. P., Motta, S. E., et al. 2020, NatAs, 4, 697
Bright, J. S., Rhodes, L., Farah, W., et al. 2023, NatAs, 7, 986
Brocksopp, C., Fender, R. P., McCollough, M., et al. 2002, MNRAS, 331, 765
Burridge, B. J., Miller-Jones, J. C. A., Bahramian, A., et al. 2025, arXiv:2502.
Carotenuto, F., Corbel, S., Tremou, E., et al. 2021, MNRAS, 504, 444
Carotenuto, F., Fender, R., Tetarenko, A. J., et al. 2024, MNRAS, 533, 4188
Carotenuto, F., Tetarenko, A. J., & Corbel, S. 2022, MNRAS, 511, 4826
CASA Team, Bean, B., Bhatnagar, S., et al. 2022, PASP, 134, 114501
Corbel, S., Coriat, M., Brocksopp, C., et al. 2013, MNRAS, 428, 2500
Corbel, S., & Fender, R. P. 2002, ApJL, 573, L35
Corbel, S., Fender, R. P., Tzioumis, A. K., et al. 2002, Sci, 298, 196
Coriat, M., Corbel, S., Prat, L., et al. 2011, MNRAS, 414, 677
Corral-Santana, J. M., Casares, J., Muñoz-Darias, T., et al. 2016, A&A,
   587, A61
De Colle, F., & Lu, W. 2020, NewAR, 89, 101538
Draghis, P. A., Miller, J. M., Homan, J., et al. 2023, ATel, 16219, 1
Espinasse, M., Corbel, S., Kaaret, P., et al. 2020, ApJL, 895, L31
Fender, R. 2010, in The Jet Paradigm, ed. T. Belloni (Berlin: Springer), 115
Fender, R., & Bright, J. 2019, MNRAS, 489, 4836
Fender, R., Bright, J., Mooley, K., & Miller-Jones, J. 2019, MNRAS, 490, L76
Fender, R., Corbel, S., Tzioumis, T., et al. 1999, ApJL, 519, L165
Fender, R., Woudt, P. A., Corbel, S., et al. 2016, in MeerKAT Science: On the
   Pathway to the SKA (Trieste: SISSA), 13
Fender, R. P., Belloni, T. M., & Gallo, E. 2004, MNRAS, 355, 1105
Fender, R. P., Garrington, S. T., McKay, D. J., et al. 1999, MNRAS, 304, 865
Fender, R. P., Homan, J., & Belloni, T. M. 2009, MNRAS, 396, 1370
Gallo, E., Degenaar, N., & van den Eijnden, J. 2018, MNRAS, 478, L132
Gallo, E., Fender, R. P., & Pooley, G. G. 2003, MNRAS, 344, 60
Garrington, S., & Beswick, R. 2016, A&G, 57, 28
Gehrels, N., Chincarini, G., Giommi, P., et al. 2004, ApJ, 611, 1005
Gottlieb, O., Metzger, B. D., Quataert, E., et al. 2023, ApJL, 958, L33
Hardcastle, M. J., & Croston, J. H. 2020, NewAR, 88, 101539
Heywood, I., 2020 oxkat: Semi-automated Imaging of MeerKAT Observations,
   Astrophysics Source Code Library, ascl:2009.003
Heywood, I., Jarvis, M. J., Baker, A. J., et al. 2016, MNRAS, 460, 4433
Heywood, I., Jarvis, M. J., Hale, C. L., et al. 2022, MNRAS, 509, 2150
Hjellming, R. M., & Johnston, K. J. 1988, ApJ, 328, 600
Hjellming, R. M., & Rupen, M. P. 1995, Natur, 375, 464
Homan, J., & Belloni, T. 2005, Ap&SS, 300, 107
Hughes, A. K., Cowie, F. J., Heywood, I., & Hugo, B., 2025 polkat: Semi-
   automate full polarization of MeerKAT observations, Astrophysics Source
   Code Library, ascl:2502.026
Ingram, A. R., & Motta, S. E. 2019, NewAR, 85, 101524
Jonas, J. & MeerKAT Team 2016, in MeerKAT Science: On the Pathway to
  the SKA (Trieste: SISSA), 1
Kalemci, E., Kara, E., & Tomsick, J. A. 2022, in Handbook of X-ray and Gamma-
   ray Astrophysics, ed. C. Bambi & A. Sangangelo, Vol. 9 (Berlin: Springer)
Kennea, J. A. & Swift Team 2023, GCN, 34540, 1
Koljonen, K. I. I., Russell, D. M., Fernández-Ontiveros, J. A., et al. 2015, ApJ,
   814, 139
Krimm, H. A., Holland, S. T., Corbet, R. H. D., et al. 2013, ApJS, 209, 14
Kumar, P., & Zhang, B. 2015, PhR, 561, 1
Liu, H.-X., Xu, Y.-J., Zhang, S.-N., et al. 2024, arXiv:2406.03834
Livio, M. 2002, Natur, 417, 125
Longair, M. S. 2011, High Energy Astrophysics (3rd ed.; Cambridge:
   Cambridge Univ. Press)
```

```
498, L40
Martí-Vidal, I., Vlemmings, W. H. T., Muller, S., & Casey, S. 2014, A&A,
  563, A136
Mata Sánchez, D., Muñoz-Darias, T., Armas Padilla, M., Casares, J., &
  Torres, M. A. P. 2024, A&A, 682, L1
Mata Sánchez, D., Torres, M. A. P., Casares, J., et al. 2025, A&A, 693, A129
Matsuoka, M., Kawasaki, K., Ueno, S., et al. 2009, PASJ, 61, 999
McClintock, J. E., & Remillard, R. A. 2006, in Compact Stellar X-Ray
   Sources, ed. W. Lewin & M. van der Klis, Vol. 39 (Cambridge: Cambridge
   Univ. Press), 157
Mereminskiy, I., Lutovinov, A., Molkov, S., et al. 2024, MNRAS, 531, 4893
Migliari, S., Tomsick, J. A., Miller-Jones, J. C. A., et al. 2010, ApJ, 710, 117
Migliori, G., Corbel, S., Tomsick, J. A., et al. 2017, MNRAS, 472, 141
Mihara, T., Nakajima, M., Sugizaki, M., et al. 2011, PASJ, 63, S623
Miller-Jones, J. C. A., Bahramian, A., Altamirano, D., et al. 2023a, ATel,
  16271, 1
Miller-Jones, J. C. A., Sivakoff, G. R., Bahramian, A., & Russell, T. D. 2023b,
  ATel, 16211, 1
Miller-Jones, J. C. A., Tetarenko, A. J., Sivakoff, G. R., et al. 2019, Natur,
   569, 374
Mirabel, I. F., & Rodríguez, L. F. 1994, Natur, 371, 46
Moldon, J. 2018, 14th European VLBI Network Symp. & Users Meeting
  (EVN 2018), ed. I. Agudo, (Trieste: SISSA), 152, https://pos.sissa.it/344
Offringa, A. R., 2010 AOFlagger: RFI Software, Astrophysics Source Code
  Library, ascl: 1010.017
Pacholczyk, A. G., & Roberts, J. A. 1971, PhT, 24, 57
Page, K. L., Dichiara, S., Gropp, J. D., et al. 2023, GCN, 34537, 1
Peng, J.-Q., Zhang, S., Shui, Q.-C., et al. 2024, ApJL, 960, L17
Peters, W. M., Polisensky, E., Clarke, T. E., Giacintucci, S., & Kassim, N. E.
  2023, ATel, 16279, 1
Plotkin, R. M., Gallo, E., & Jonker, P. G. 2013, ApJ, 773, 59
Podgorny, J., Svoboda, J., & Dovčiak, M. 2024, ATel, 16541, 1
Polisensky, E., Lane, W. M., Hyman, S. D., et al. 2016, ApJ, 832, 60
Ruiz, M., Shapiro, S. L., & Tsokaros, A. 2021, FrASS, 8, 39
Rushton, A. P., Miller-Jones, J. C. A., Curran, P. A., et al. 2017, MNRAS,
  468, 2788
Russell, D. M., Fender, R. P., Hynes, R. I., et al. 2006, MNRAS, 371, 1334
Russell, D. M., Maitra, D., Dunn, R. J. H., & Markoff, S. 2010, MNRAS,
  405, 1759
Russell, D. M., Markoff, S., Casella, P., et al. 2013, MNRAS, 429, 815
Russell, T. D., Carotenuto, F., Miller-Jones, J. C. A., et al. 2024, ATel,
  16552, 1
Russell, T. D., Lucchini, M., Tetarenko, A. J., et al. 2020, MNRAS, 498, 5772
Russell, T. D., Soria, R., Miller-Jones, J. C. A., et al. 2014, MNRAS,
  439, 1390
Russell, T. D., Tetarenko, A. J., Miller-Jones, J. C. A., et al. 2019, ApJ,
Sánchez-Sierras, J., & Muñoz-Darias, T. 2020, A&A, 640, L3
Sault, R. J., Teuben, P. J., & Wright, M. C. H. 1995, in ASP Conf. Ser. 77,
  Astronomical Data Analysis Software and Systems IV, ed. R. A. Shaw,
  H. E. Payne, & J. J. E. Hayes (San Francisco, CA: ASP), 433
Shahbaz, T., Russell, D. M., Zurita, C., et al. 2013, MNRAS, 434, 2696
Shapiro, S. L., Lightman, A. P., & Eardley, D. M. 1976, ApJ, 204, 187
Svoboda, J., Dovčiak, M., Steiner, J. F., et al. 2024, ApJL, 966, L35
Tananbaum, H., Gursky, H., Kellogg, E. M., et al. 1972, ApJL, 174, L143
Tetarenko, A. J., Freeman, P., Rosolowsky, E. W., Miller-Jones, J. C. A., &
  Sivakoff, G. R. 2018, MNRAS, 475, 448
Tetarenko, A. J., Sivakoff, G. R., Miller-Jones, J. C. A., et al. 2017, MNRAS,
  469, 3141
Tetarenko, B. E., Sivakoff, G. R., Heinke, C. O., & Gladstone, J. C. 2016,
   ApJS, 222, 15
Thorne, K. S., & Price, R. H. 1975, ApJL, 195, L101
van der Laan, H. 1966, Natur, 211, 1131
Wood, C. M., Miller-Jones, J. C. A., Homan, J., et al. 2021, MNRAS,
  505, 3393
Wood, C. M., Miller-Jones, J. C. A., Bahramian, A., et al. 2024, ApJ, 971,
Wood, C. M., Miller-Jones, J. C. A., Bahramian, A., et al. 2025, ApJ, 984, L53
Yu, W. 2023, ATel, 16276, 1
```

Maccarone, T. J., Osler, A., Miller-Jones, J. C. A., et al. 2020, MNRAS,